Available online at www.sciencedirect.com
SCIENCE DIRECT®
PERGAMON
International Journal of Multiphase Flow 29 (2003) 435–460
International Journal of Multiphase Flow
www.elsevier.com/locate/ijmulflow

A numerical study of the interfacial transport characteristics outside spheroidal bubbles and solids

W.Z. Li [a], Y.Y. Yan [a,*], J.M. Smith [b]

[a] School of Engineering, The Nottingham Trent University, Burton Street, Nottingham NG1 4BU, UK
[b] Department of Chemical and Process Engineering, The University of Surrey, Guilford GU2 7XH, UK

Received 14 June 2002; received in revised form 25 November 2002

Abstract

In this paper, the interfacial transport characteristics to or from spheroidal bubbles are studied numerically and the results of numerical simulations are reported. The numerical modelling uses the SIMPLE method with a non-orthogonal, boundary fitted staggered grid. The aim of this paper is to provide an understanding of the interfacial transport characteristics of inviscid spheroidal bubbles, of different geometric parameters, rising in a stagnant hot or bi-solution liquid. The flow and concentration (or temperature) fields around bubbles and similarly sized rigid spheroids are computed. Detailed analyses of the pressure and vorticity distributions at surfaces of the inviscid spheroidal bubbles are made and compared with those of similar rigid spheroids. Drag coefficients for and wake lengths behind rigid spheroids and inviscid spheroidal bubbles are also presented. Local and mean Sherwood numbers and Nusselt numbers at bubble and rigid spheroid surfaces are compared, as well as their change with the Reynolds and Schmidt numbers and geometric parameters.

Keywords: Spheroidal bubble; Rigid spheroids; Numerical simulation; Interfacial transport characteristics; Non-orthogonal BFCs

1. Introduction

It is important to understand the motion and interfacial transport around a bubble or solid particle moving through a stagnant hot or bi-solution liquid since such conditions arise in such industrial processes as water treatment, metallurgy, pharmaceutical production and a variety of

* Corresponding author. Fax: +44-115-848-6506.
E-mail address: yuying.yan@ntu.ac.uk (Y.Y. Yan).

0301-9322/03/$ - see front matter
doi:10.1016/S0301-9322(02)00163-5

chemical processes. The heat and mass transfer processes are also relevant to the generation and motion of bubbles in boiling systems in the power industry, nuclear reactors and many other situations. For example, in a chemical reactor with bubbly flow, the production capacity depends on the heat and mass transfer at the liquid–gas interface. The investigation on the characteristics of interfacial transport to or from bubbles has long been a challenging subject. A recent numerical study of the flow, heat and mass transfer at surface of an inviscid spherical bubble has been carried out (Yan and Li, 2002). As stated there, although many researchers have considered bubbles as spherical, which is reasonably true for small bubbles, this is not the case for larger bubbles developed in some applications and conditions. Because an irregular body is more difficult to treat computationally using a conventional Cartesian, cylindrical polar or spherical polar coordinate system, numerical procedures for solving the full Navier–Stokes equations on non-orthogonal boundary fitted coordinates (BFCs) have been proposed in the past decade. Due to the advantages of such BFCs, they are employed in the present work to match the boundaries of a bubble that is not assumed to be spherical, described by a range of geometric parameters.

Modern computers offer the possibility of solving the full Navier–Stokes equations; so that numerical simulations of separated flows past a spheroid have been carried out for years. Masliyah and Epstein (1970) carried out a numerical study on flow past a rigid spheroid and achieved some useful results for mass transfer for $Re \leqslant 100$. In their work, the Navier–Stokes equation was transformed into a form of vorticity-stream function based on spheroidal coordinates to match spheroidal boundary conditions and was discretised by means of the finite difference method. In the mean time, some researchers also used boundary layer theory to simplify the Navier–Stokes equation in order to find the solution for the governing flow past rigid spheroids; these can be seen in the works by Wang et al. (1990), Wu and Shen (1992), Cebeci and Su (1988) and Patel and Baek (1985). Regarding a two-dimensional axisymmetric flow, a method based on the stream function and vorticity has been employed to provide a transform of the Navier–Stokes equation. This avoids the need to solve the pressure gradient in incompressible flow problems directly. Ryskin and Leal (1984a,b,c) used this method to simulate bubble motion in a stagnant liquid. Patankar and Spalding (1972) and Patankar (1980) developed the SIMPLE algorithm in which the velocity and pressure are solved directly. Tomiyama et al. (1994) used this method to calculate three-dimensional rising bubbles by employing a rectangular grid system fixed in physical space. Takagi and Matsumoto (1996) carried out full simulations for a spherical bubble rising through a quiescent liquid. Recently, Takagi et al. (1997) simulated an unsteady axisymmetric flow with a free surface using orthogonal BFCs.

However, these numerical investigations on the motion of bubble through a stagnant liquid are limited to solving the flow field only. Few papers have considered the heat or mass transfer associated with flow past spheroidal bubbles with different geometric parameters. Although experimental studies dealing with heat and mass transfer can be found in Clift et al. (1978), they are limited to providing correlations between mass transfer factors and equivalent diameters. It is well known that as a vapour bubble rises through a stagnant hot or cold liquid the motion is always accompanied by heat and mass transfer across the interface. Based on the Stefan boundary condition at the liquid and gas interface, the temperature and concentration gradients at the interface are the main transport characteristics. The gradients can be described in terms of dimensionless local Nusselt and Sherwood numbers. Understanding the way these groups vary from point to point around the interface is of fundamental importance for the simulation of the growth

or collapse of a bubble as it rises through stagnant hot or cold liquid. Therefore, the first aim of this paper is to numerically study the characteristics of heat and mass transfer at the interface. As far as the method is concerned, orthogonal curvilinear BFCs have been employed for many previous simulations. However, the orthogonality severely constrains a two-dimensional grid in a simple geometric domain and is generally impossible to achieve in three-dimensions (Huang and Prosperetti, 1994). The other aim of this paper is to examine the adaptability and potential of non-orthogonal BFCs for solve full Navier–Stokes equations for the flow past non-spherical particles. Accordingly, the numerical investigations of flow and heat mass transfer provide fundamental information for further investigation of rising bubbles. In the present work, a mathematical formulation describing the phenomena with non-orthogonal BFCs is proposed. An improved SIMPLE algorithm suitable for the non-orthogonal BFCs has been successfully developed and validated. The earlier and present numerical simulations of the flow and heat transfer at the interface of a spherical bubble are compared. These results are considered to provide a good basis for further research.

2. Numerical method

2.1. Governing equations and their discretisation

The problem of determining the flow and heat and mass transfer between a bubble and a liquid in uniform external flow around it requires the solution of the steady axisymmetric Navier–Stokes energy and species continuity equations. In the present study, a formulation using primitive velocity and pressure variables on non-orthogonal BFCs is adopted. On this basis, the equations are written in general non-orthogonal coordinates instead of the usual general curvilinear orthogonal coordinates. These computational choices give a lot of flexibility and allow the present code to be used for solving many flow and heat transfer problems in arbitrary computational domains with complicated boundary geometries. In a non-orthogonal coordinate system there are several options for grid arrangement and the choice of the dependent variables in the momentum equations. Wang and Satoru (1999) compared solutions based on the Cartesian and covariant velocities as the dependent variables and showed that the two approaches have the same numerical accuracy. The convergence range of the relaxation factor for pressure in the covariant velocity method is quite narrow, although the convergence rate can be faster than that of Cartesian velocity method if the relaxation factor for pressure is small enough. But momentum equations in the Cartesian velocity method show strong conservation because there are no curvilinear sources corresponding to those when the covariant velocity is used (Ferziger and Peric, 1999). In this investigation, Cartesian velocity components are chosen as dependent variables for the computation of flow and heat mass transfer at the interface of a spheroidal bubble. The flow field around the bubble is considered to be two-dimensional axisymmetric; the liquid phase is an incompressible Newtonian fluid. For this case the conservation equations for a general dependent variable ϕ in a non-orthogonal coordinate system (ξ,η) can be written in the following general form:

$$\frac{\partial}{\partial\xi}r\left[\rho U\phi-\frac{\Gamma}{J}\left(\alpha\frac{\partial\phi}{\partial\xi}-\beta\frac{\partial\phi}{\partial\eta}\right)\right]+\frac{\partial}{\partial\eta}r\left[\rho V\phi-\frac{\Gamma}{J}\left(-\beta\frac{\partial\phi}{\partial\xi}+\gamma\frac{\partial\phi}{\partial\eta}\right)\right]=rJS(\xi,\eta); \tag{1}$$

where

$$U = u\frac{\partial r}{\partial \eta} - v\frac{\partial x}{\partial \eta}; \tag{2}$$

$$V = v\frac{\partial x}{\partial \xi} - u\frac{\partial r}{\partial \xi}; \tag{3}$$

$$\alpha = \left(\frac{\partial x}{\partial \eta}\right)^2 + \left(\frac{\partial r}{\partial \eta}\right)^2; \tag{4}$$

$$\beta = \frac{\partial x}{\partial \xi}\frac{\partial x}{\partial \eta} + \frac{\partial r}{\partial \xi}\frac{\partial r}{\partial \eta}; \tag{5}$$

$$\gamma = \left(\frac{\partial x}{\partial \xi}\right)^2 + \left(\frac{\partial r}{\partial \xi}\right)^2; \tag{6}$$

$$J = \frac{\partial x}{\partial \xi}\frac{\partial r}{\partial \eta} - \frac{\partial x}{\partial \eta}\frac{\partial r}{\partial \xi}; \tag{7}$$

where $S(\xi, \eta)$ is the source of ϕ in the (ξ, η) coordinates, U and V are the contravariant velocity components, α, β and γ are metric tensors and J is the Jacobian transformation number.

In this paper, a finite-volume method has been employed to discretise the governing equations. A staggered grid arrangement is used in which the scalar quantities are located at the geometric centre of a control volume, while the velocity components are displaced in two coordinate directions which lie respectively at the midpoints of the control-volume faces. The details can be found in the work of Shyy et al. (1996).

2.2. Boundary conditions

In this simulation, boundary conditions at the inlet of the domain are

$$u = V_\infty, \tag{8a}$$

$$v = 0, \tag{8b}$$

$$T = T_\infty \quad \text{for a heat transfer problem,} \tag{8c}$$

$$C = C_\infty \quad \text{for a mass transfer problem.} \tag{8d}$$

The conditions at the domain outlet set the normal velocity gradient and tangential velocity equal to zero,

$$\frac{\partial u}{\partial x} = 0, \quad v = 0, \quad \frac{\partial T}{\partial x} = 0, \quad \frac{\partial C}{\partial x} = 0. \tag{9a, b, c, d}$$

Due to the assumption of axisymmetric flow, symmetric boundary conditions are

$$\frac{\partial u}{\partial r} = 0, \quad v = 0. \tag{10a, b}$$

No-slip conditions are imposed on the surface of the rigid sphere, i.e.

$$u = 0, \quad v = 0, \quad T = T_s, \quad C = C_s. \tag{11a, b, c, d}$$

Whereas the bubble surface is considered to be a shear-free interface where the normal velocity equals zero, i.e.

$$\tau_\tau = \mu\left[x_\xi\gamma\frac{\partial u}{\partial\eta} - (x_\xi\beta + r_\xi J)\frac{\partial u}{\partial\xi} + (x_\xi J - r_\xi\beta)\frac{\partial v}{\partial\xi} + r_\xi\gamma\frac{\partial v}{\partial\eta}\right]_b = 0, \tag{12a}$$

$$\frac{v_b x_\xi - u_b r_\xi}{\sqrt{\gamma}} = 0; \tag{12b}$$

where subscript b stands for values at the interface.

2.3. The bubble shape and grid generation

In this paper, both the inviscid bubble and the rigid body are considered to be spheroids with a range of possible geometric parameters. In most systems, bubbles in the intermediate size range (d_e typically between 1 and 15 mm) lie in this regime (Clift et al., 1978). Fig. 1 gives the geometric parameters used for the bubble and rigid spheroid. Where B is a semimajor axis and A is semi-minor axis. Conventionally, the eccentricity E is used to define a shape factor:

$$E = \frac{A}{B}. \tag{13}$$

For the non-spherical bodies, a non-orthogonal body fitted coordinate system has been employed. The numerical grid generation technique developed by Thompson et al. (1974) has been used. In the present research, the technique for generating the transformed coordinate as solutions of an elliptic differential system in the physical space has been applied to a single-connected region with arbitrarily shaped bubbles. The point (x, r) in physical space satisfies the following elliptic equations in the non-orthogonal BFC system (ξ, η):

$$\alpha\frac{\partial^2 f}{\partial\xi^2} - 2\beta\frac{\partial^2 f}{\partial\xi\partial\eta} + \gamma\frac{\partial^2 f}{\partial\eta^2} + J^2\left(P\frac{\partial f}{\partial\xi} + Q\frac{\partial f}{\partial\eta}\right) = 0, \tag{14}$$

where $f \equiv x$ or r. Subject to appropriate boundary conditions, the mathematical problem defined by Eq. (14) constitutes the boundary value problem for numerical grid generation. In the present calculations, the grid control function P and Q of Eq. (14) are determined using the method proposed by Thomas and Middelcoff (1980). The advantages of this method are that it generates a

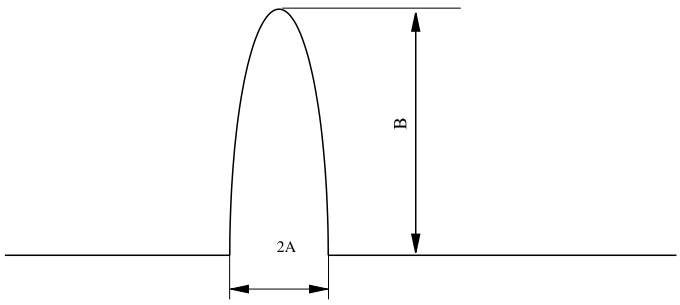

Fig. 1. Bubble shape and geometry parameters.

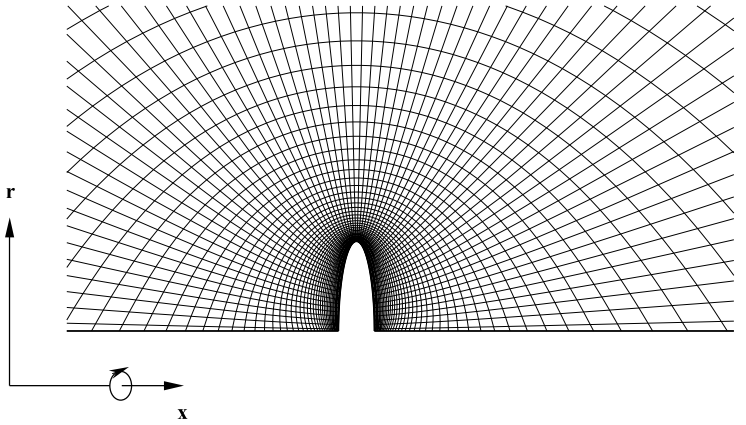

Fig. 2. Coordinate system and grid generation.

grid which is normal to the physical boundary and that it is easy to control the grid concentration in the computational domain. Since the problem is assumed to be axisymmetric, the single-connected region in physical space is transformed into a single-connected region in computational space, as shown in Fig. 2.

3. Preliminary testing

Before being used to compute flows past spheroidal bubbles or rigid spheroids with differing E, the code was extensively tested. In this paper, the results of two validation problems are presented. One is the classical external flow past a rigid sphere. The other is a flow past a rigid spheroid. In the first test problem, some existing numerical results using various methods with different coordinate systems have been chosen to provide benchmark solutions for this work. They can be found in the references to Rimon and Cheng (1969), LeClair et al. (1970), Dennis and Walker (1971), Fornberg (1988) and Magnaudet et al. (1995). However, it is both necessary and important to validate the numerical method and code developed for the simulation of heat and mass transfer at the interface of spheroidal bubble. Several tests were carried out to determine the adaptive characteristics of the grid to be used for simulating the flow around a spherical solid or bubble at $Re = 1$, 10, 100 and 200. In this work, the optimal size of the computational domain and grid type has been tested at different Reynolds number. To avoid confinement effects in low-Re flows as stated by Magnaudet et al. (1995), it was found that for spheroids the radial computational boundary should be at 80 equivalent radii ($0.5d_e$). With the C-type grid, the number of grid points was determined by comparing different grid arrangements to ensure the solution to be grid-independent. The results of calculations of vorticity, pressure and local Sherwood number distributions based on trials with 45×45, 66×66 and 91×91 grids are shown in Fig. 3 (where the vorticity and pressure are normalised by $2V_\infty/d$ and $0.5\rho V_\infty^2$, respectively). It is clear that there is no significant improvement is achieved by refining the grid beyond 66×66 and that at this level the results at $Re = 100$ are consistent with those of Magnaudet et al. (1995). The 66×66 grid is

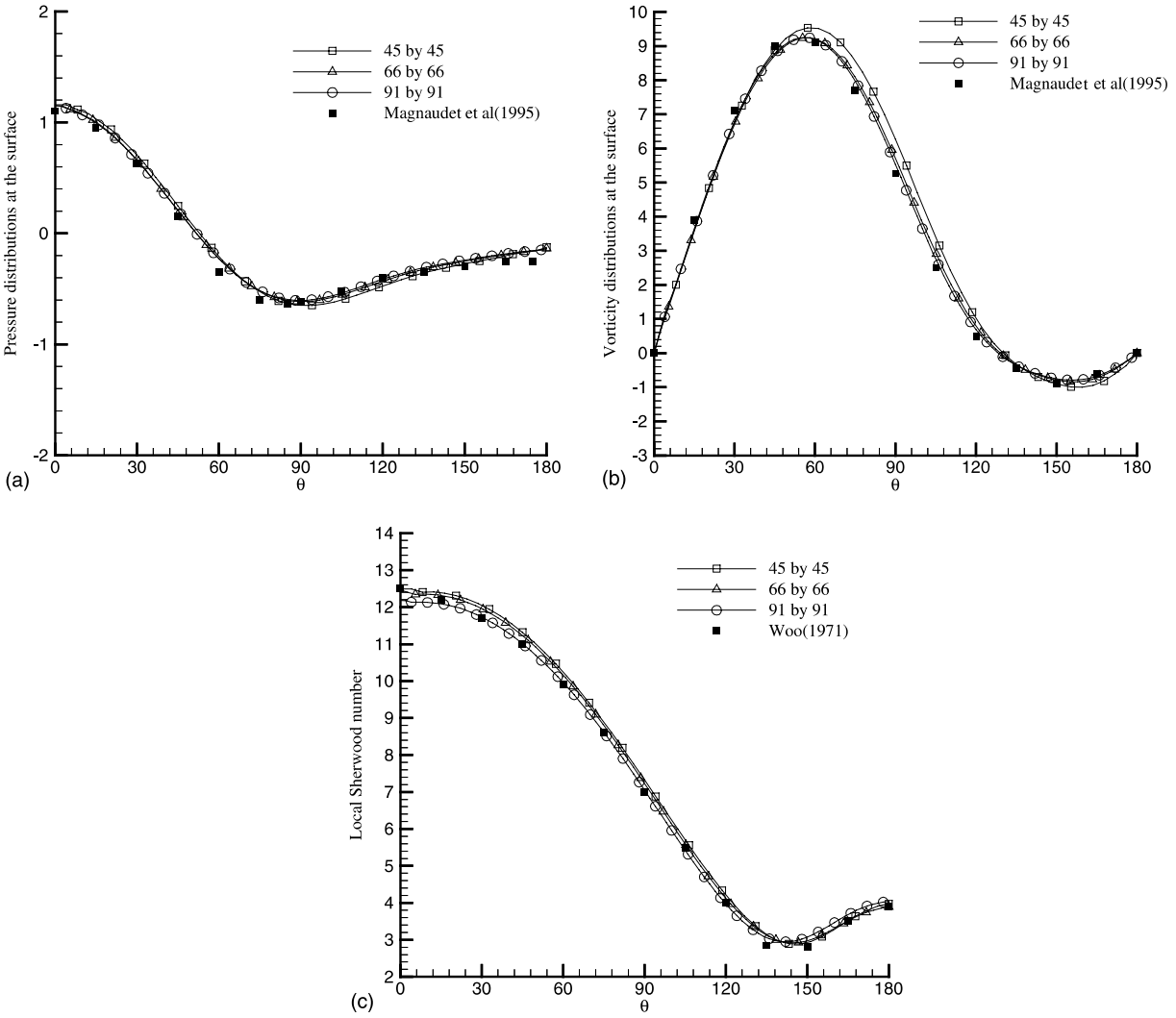

Fig. 3. (a) Comparison of surface pressure distributions for rigid sphere in different grid number (at $Re = 100$). (b) Comparison of surface vorticity distributions for rigid sphere in different grid number (at $Re = 100$). (c) Comparison of surface local Sherwood (or Nusselt) number for rigid sphere in different grid number (at $Re = 100$).

employed in all cases in the present simulation. Fig. 4 present comparisons of drag coefficients and wake length between the present results and others for a rigid sphere. It can be seen from Fig. 4a that there is no significant difference between present results and LeClair et al. (1970) and Magnaudet et al. (1995) results. It is also seen from Fig. 4b that present wake lengths are consistent with those of LeClair et al. (1970) and Rimon and Cheng (1969).

The grid concentration in vicinity of the bubble surface has been tested. The growth ratio of the grid is 1.125 for all cases in the present work. This growth ratio is big enough to guarantee that the thickness of the first row cells around the bubble is less than boundary layer of concentration. For the computations of the flow past a rigid sphere, the Reynolds number is only taken up to 200.

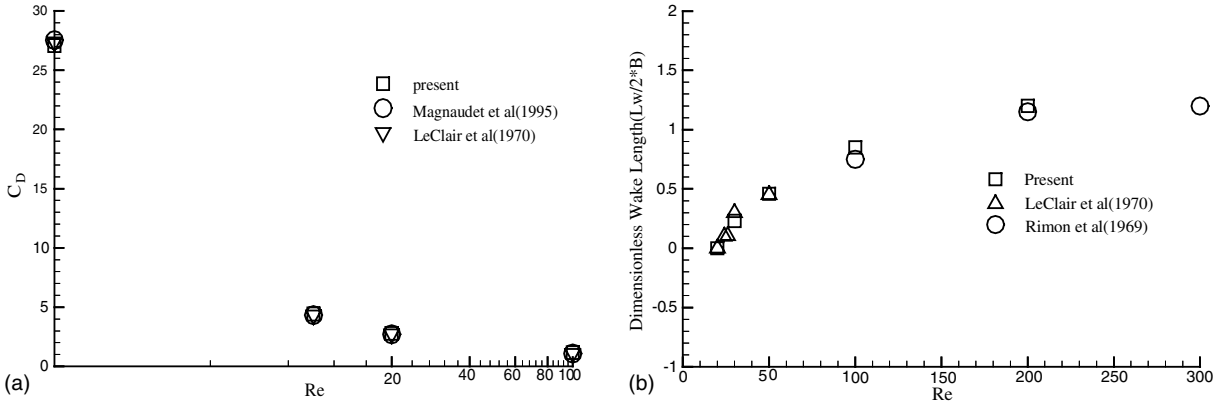

Fig. 4. (a) A comparison of drag coefficients between the present results and others for a rigid sphere ($E = 1$). (b) A comparison of wake length between the present results and others for a rigid sphere ($E = 1$).

This limit corresponds roughly to the transition region between axisymmetric flow and the non-axisymmetric vortex shedding regime for a rigid sphere (Magnaudet et al., 1995).

The second test problem is that of flow past rigid spheroids with differing eccentricities. Many researchers have used boundary layer theory to simplify the Navier–Stokes equations (Wang et al., 1990; Wu and Shen, 1992; Cebeci and Su, 1988; Patel and Baek, 1985). Few numerical and experimental data with bubbles are available in the literature for comparison, although Ryskin and Leal (1984a,b,c) and Takagi et al. (1997) studied numerically the motion of bubbles of different shapes. Numerical results for the flow past a rigid spheroid will therefore be used to validate the present results. Fig. 5 compare the present results with the work of Masliyah and Epstein

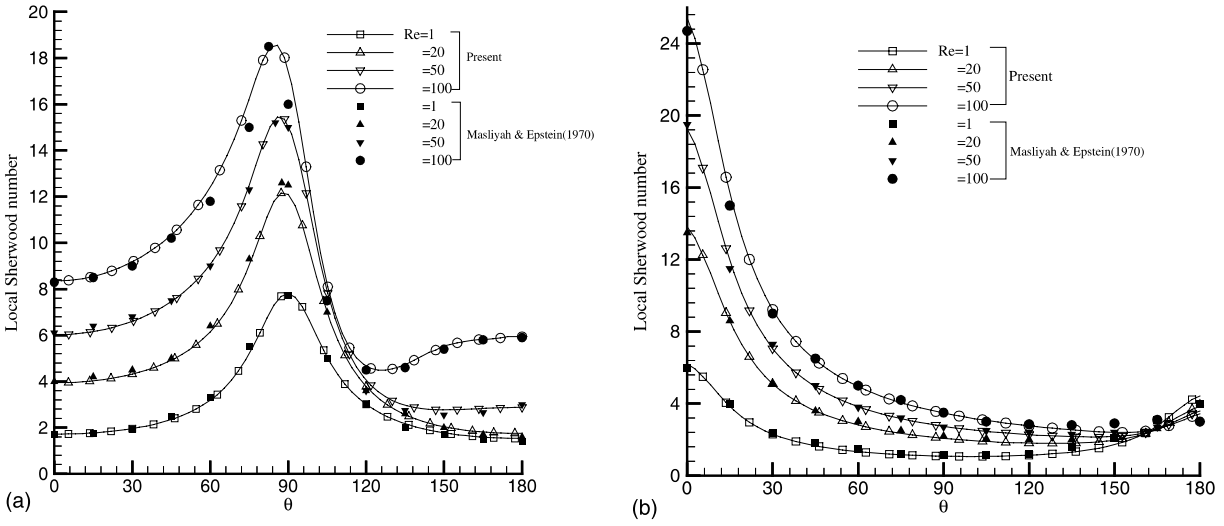

Fig. 5. (a) The local Sherwood number comparison of the present and Masliyah and Epstein (1972) at $E = 0.2$. (b) The local Sherwood number comparison of present and Masliyah and Epstein (1972) at $E = 5$.

(1972). It can be seen that present calculations of Sherwood number distributions at various Reynolds numbers are in very good agreement.

4. Numerical results and analysis

The inviscid bubble and the rigid body are each assumed to be a spheroid with an eccentricity E. They are moving at a constant velocity V in a stagnant incompressible Newtonian fluid of viscosity μ, and density ρ. The interface of the bubble is assumed to be shear-free at the surface of bubble. In the case studied, Reynolds number is defined as $Re = 2\rho VB/\mu$. Since the dimensionless equations and boundary conditions governing heat and dilute-solution mass transfer are identical, the solutions to these equations in dimensionless form are also identical. Profiles of dimensionless concentration and temperature are therefore the same, while the dimensionless transfer rates, the Sherwood number ($Sh = 2\hbar B/\text{ƛ}$) for mass transfer, and the Nusselt number ($Nu = 2hB/k$) for heat transfer, are identical functions of Re, Sc ($= \nu/\text{ƛ}$) or Pr ($= \nu/a$). In this simulation, the Reynolds number is set at 1, 10, 20, 30, 50 and 100 respectively, low enough to avoid vortex shedding. As the flow around a rigid spheroid at $Sc = 0.7$ has been well simulated, producing what are regarded as benchmark solutions (Magnaudet et al., 1995), similar conditions are employed in the present simulations of an inviscid fluid spheroid, which may be regarded as a pseudo spheroidal bubble. By comparing with the benchmark solutions for the solid spheroid at $Sc = 0.7$, the results for the same scale fluid spheroid may best demonstrate the difference between the fields around a solid and the fluid spheroid and can test the feasibility of the numerical method for modelling of a fluid spheroid in liquid with an interface of which the fluid (the gas) inside the bubble is inviscid, even though the condition $Sc = 0.7$ is of limited practical interest. For an inviscid bubble at low Reynolds number ($Re = 10$), the changes of Sh with Sc (Sc is set at 0.5, 5, 50, 500 and 1000 respectively) and eccentricity parameter E (E is set at 0.2, 0.5 and 1.0 respectively) have also been calculated and presented.

4.1. Fields around the spheroidal particles

Fig. 6 shows streamlines and concentration contours for flow past spheroids at $Re = 100$. The present results for global fields around rigid spheroids are in very good agreement with those of Masliyah and Epstein (1970). As the body becomes more 'streamlined' (as E increases), the wake volume decreases; in particular, at $E = 5$, there is no wake at $Re = 100$. This is also true for inviscid bubbles; as it is seen in Fig. 7, the wake volume decreases with E; when the bubble is spherical, $E = 1.0$, there is no separation at the rear of the bubble. Figs. 8 and 9 show streamlines and concentration contours for a rigid spheroid and an inviscid spheroidal bubble of $E = 0.2$ at different Reynolds numbers. In these figures dashed lines represent the concentration contours and solid lines denote streamlines. The wake volume is small at the rear of the rigid spheroid even at low Reynolds numbers when E is small; this is seen in Fig. 8b. This is very different from the result computed for a rigid sphere (Yan and Li, 2002). When Re is small, the concentration (and similarly the temperature) contours are nearly uniform distributions in all directions around both spheroidal bubbles and solids. This is because convection is weaker than mass or thermal diffusion. At Reynolds numbers above 10, the wake exists at the rear of the spheroids and the

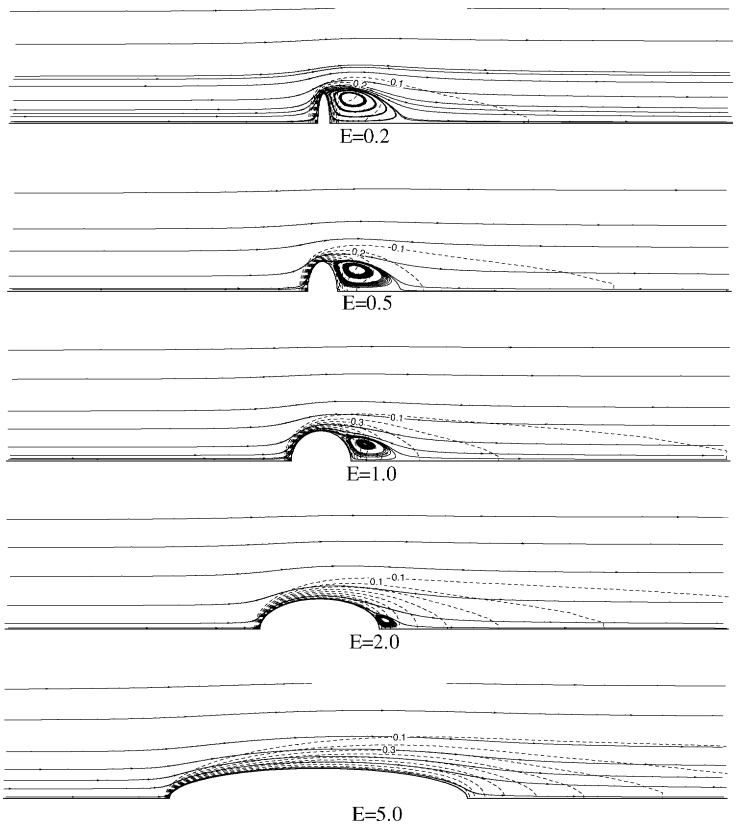

Fig. 6. Streamlines and concentration contours for flow past rigid spheroids at $Re = 100$, where dashed lines stand for concentration contours and solid lines denote streamlines.

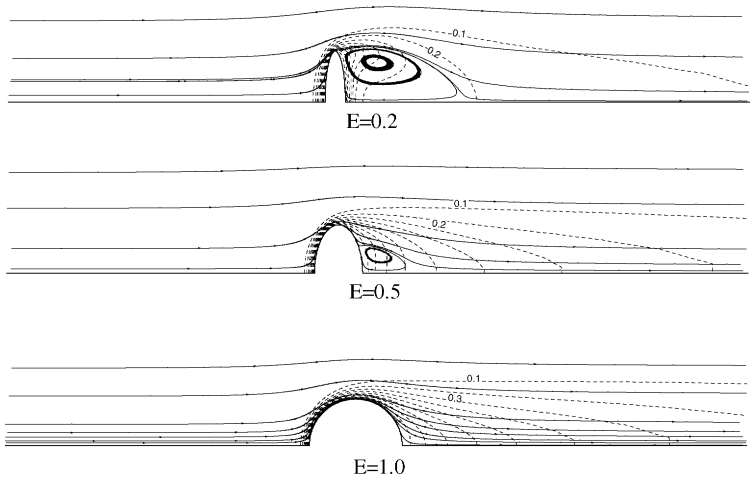

Fig. 7. Streamlines and concentration contours for flow past spheroidal bubbles at $Re = 100$, where dashed lines stand for concentration contours and solid lines denote streamlines.

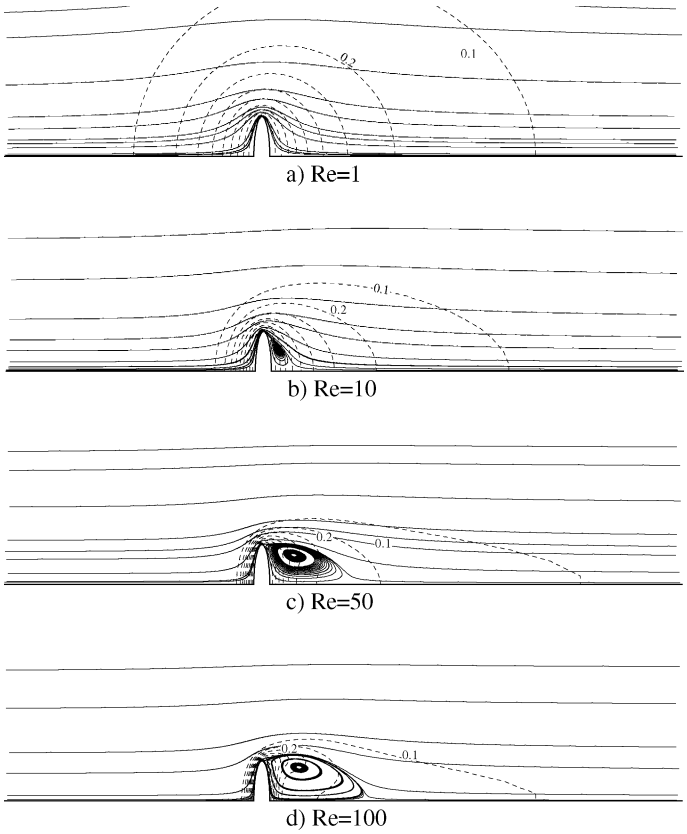

Fig. 8. The streamlines and concentration contours for rigid spheroid at $E = 0.2$, where dashed lines stand for concentration contours and solid lines denote streamlines.

concentration distributions become increasingly asymmetric. Increasing Reynolds number enhances convection so that mass or heat is transported back towards the rear of the body. As a result, a region of high concentration or temperature develops behind the bodies. Furthermore, the separation angle on rigid spheroids is different from that for the inviscid spheroidal bubbles. The separation angle for rigid spheroids is always sited at the edge of the spheroid (based on the semimajor axis), while it for bubbles is located at a point behind the edge, regardless of how high the Reynolds number is.

Figs. 10 and 11 show the computed streamlines and concentrations or temperature fields for rigid spheroids and inviscid spheroidal bubbles of $E = 0.5$ at different Reynolds number. In contrast to the results with E near to 1, when the shapes of streamlines and contours are similar for both bubbles and particles, there are now marked differences in the streamlines and contours. For an inviscid bubble, the wake volume at rear of the bubble is smaller than that behind rigid spheroids at the same Reynolds number. The separation angle for rigid spheroids is bigger than that for inviscid spheroidal bubbles. It is also found that the separation angle for a bubble changes with E at same Reynolds number.

In view of the above comparisons (in Figs. 6–11) for rigid spheroids and spheroidal bubbles, we can find that the physics involved in the generation of recirculating region is somewhat different

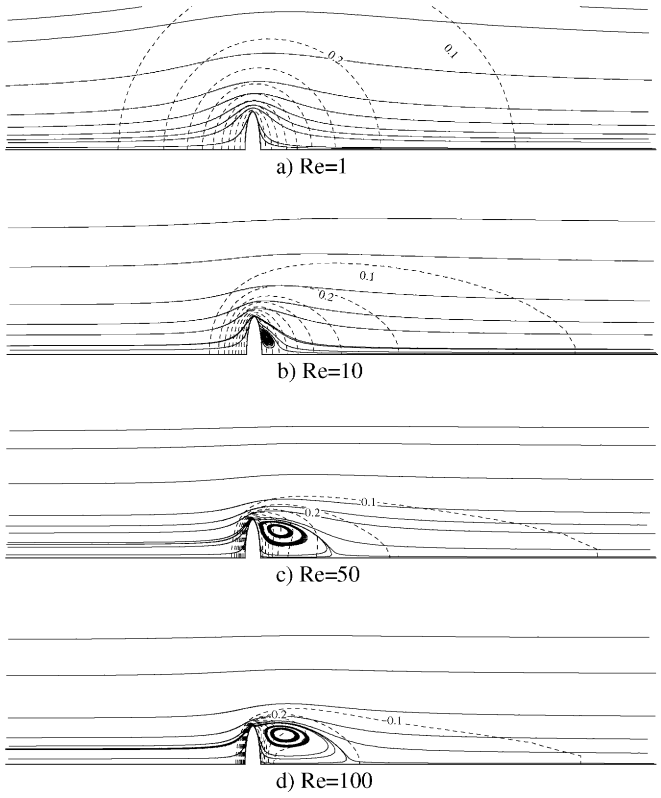

Fig. 9. The streamlines and concentration contours for spheroid bubble at $E = 0.2$, where dashed lines stand for concentration contours and solid lines denote streamlines.

for the two types of bodies. For the spheroidal bubble, even though the surface is shear-free, the curvature produces vorticity, whereas on a rigid body surface the vorticity is directly proportional to the local shear. This difference in the way that vorticity is generated at the surface explains why the wake is much longer for a rigid spheroid than for a bubble for given E and Re.

The concentration fields of solids or bubbles with eccentricities 0.2 and 0.5 show strikingly large differences. The volume within which there are significant concentration or temperature changes is much bigger behind a bubble than behind a solid. The concentration boundary layer around a rigid spheroid is thicker than that around a bubble. The velocity boundary layer that develops around a rigid spheroids results in a thicker layer of concentration or temperature boundary. Furthermore, separating flow always occurs at the rear of rigid spheroids, developing a vortex in the low velocity region which further thickens the concentrations or temperature boundary layer.

Fig. 12 compares the pressure contours for inviscid spherical and spheroidal bubbles at $Re = 50$ and 100. It can be seen from the figure that the eccentricity has a considerable influence on the fields. Near the spherical bubble the pressure contours are relatively symmetrical in both upstream and downstream regions while for the spheroidal bubble they become very asymmetric, especially at the higher Reynolds number of 100. The dimensionless pressure in front of the spheroidal bubble is positive, while it is negative at rear of the bubble. For the spherical bubble, there is a

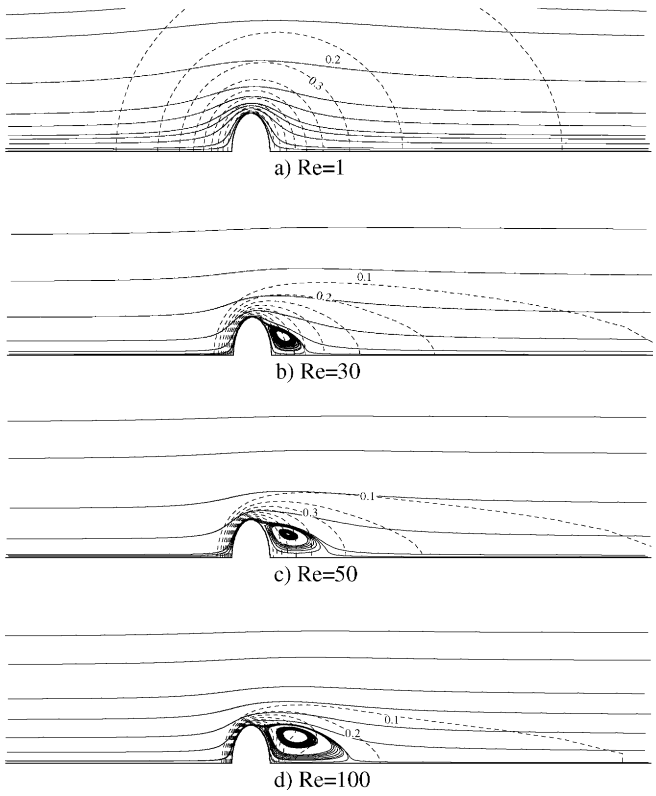

Fig. 10. The streamlines and concentration contours for the rigid spheroid at $E = 0.5$, where dashed lines stand for concentration contours and solid lines denote streamlines.

negative pressure distribution over the range from 45° to 135°. Therefore, it is clear that the bubble shape does affect the flow characteristics.

4.2. Vorticity and pressure distributions

The best way to analyse these differences is to examine precisely the distributions of vorticity and pressure at the surface. The vorticity can be defined as

$$\omega = \frac{1}{J}(u_\eta x_\xi - u_\xi x_\eta + v_\xi y_\eta - v_\eta y_\xi). \tag{15}$$

The pressure at the surface is defined as

$$p_w = p - p_\infty; \tag{16}$$

where p_∞ denotes a pressure reference chosen at the upstream boundary. For sake of convenience, interfacial vorticities and pressure shown in the figures are normalised by $2V_\infty/d_e$ and $0.5\rho V_\infty^2$ respectively.

Vorticities and pressures at the surfaces of rigid spheroids and invisicid spheroidal bubbles of $E = 0.2$ are shown in Figs. 13a,b and 14a,b at $Re = 1$, 10, 30, 50 and 100, respectively. These

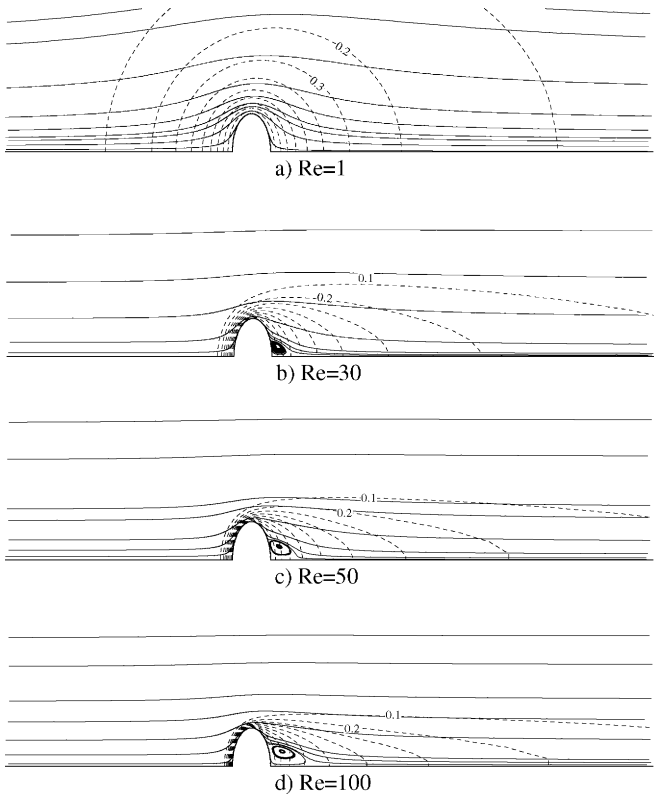

Fig. 11. The streamlines and concentration contours for the spheroidal bubble at $E = 0.5$, where dashed lines stand for concentration contours and solid lines denote streamlines.

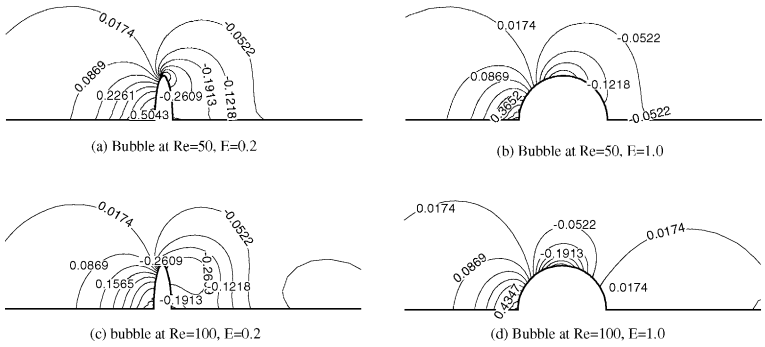

Fig. 12. Comparison of pressure contours for spheroidal and spherical bubbles.

distributions are also shown in Figs. 15a,b and 16a,b for particles in the same *Re* range and $E = 0.5$. From these distributions, there are remarkable differences between the rigid spheroids and the inviscid spheroidal bubbles. For the bubble as $Re \geqslant 50$, surface vorticity and pressure distributions remain symmetric with respect to a polar angle of 90°. It needs to be pointed out that

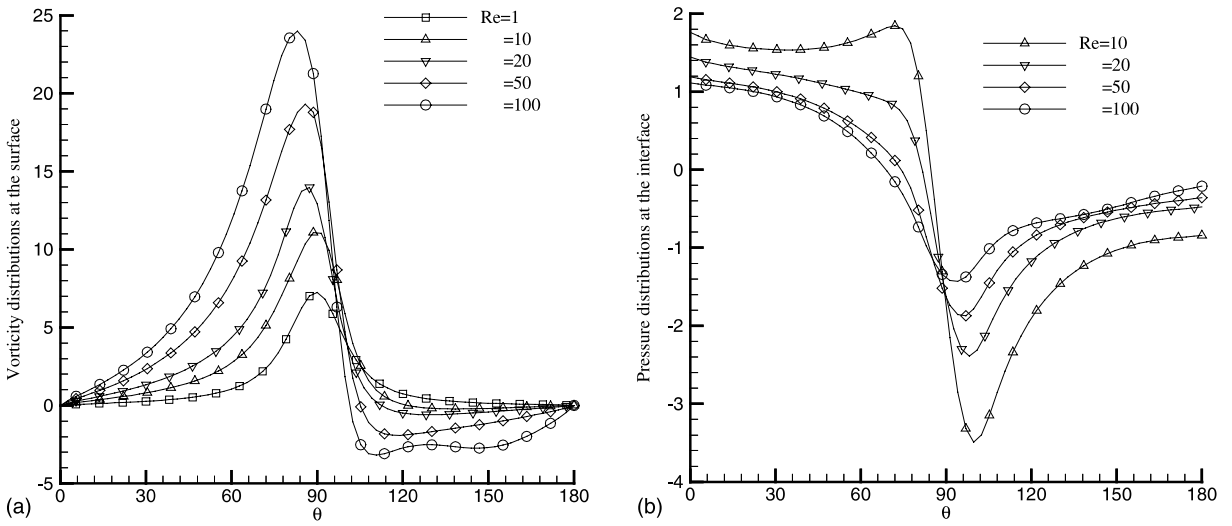

Fig. 13. (a) Surface vorticity distributions for rigid spheroid at $E = 0.2$. (b) Surface pressure distributions for rigid spheroid at $E = 0.2$.

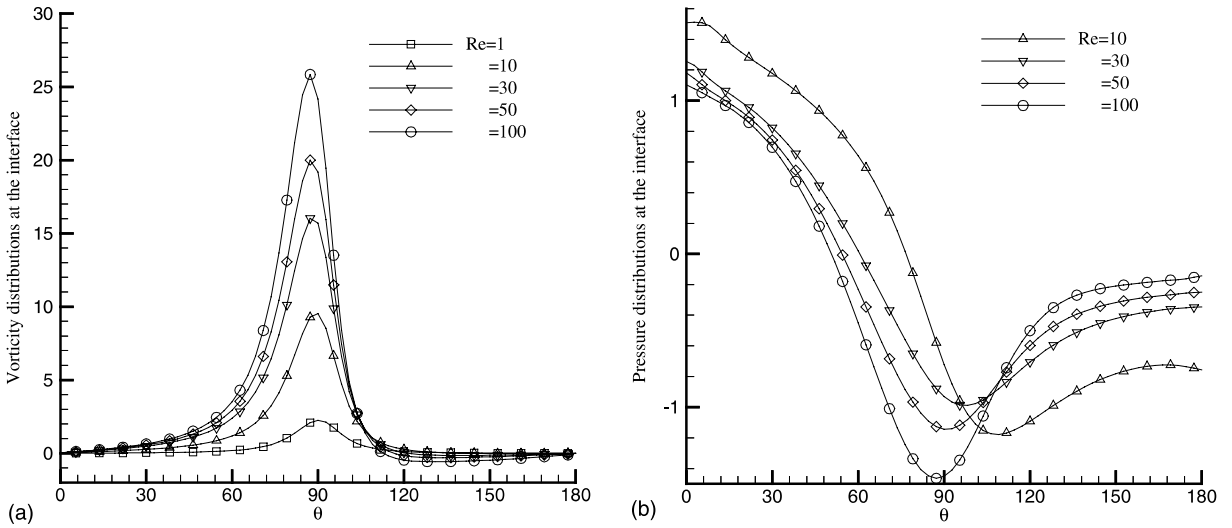

Fig. 14. (a) Surface vorticity distributions for the spheroidal bubble at $E = 0.2$. (b) Surface pressure distributions for spheroidal bubble at $E = 0.2$.

the pressure distributions for $Re = 1$ have not been plotted in these figures since they have larger pressure differences.

At $Re \leqslant 10$, pressure distributions at the surface for rigid spheroids and inviscid bubbles are different from those when Re is high. Pressure values at the front stagnation point at $Re = 10$ are bigger than those when Re is high. When Re is increased, the profiles of the pressure distribution

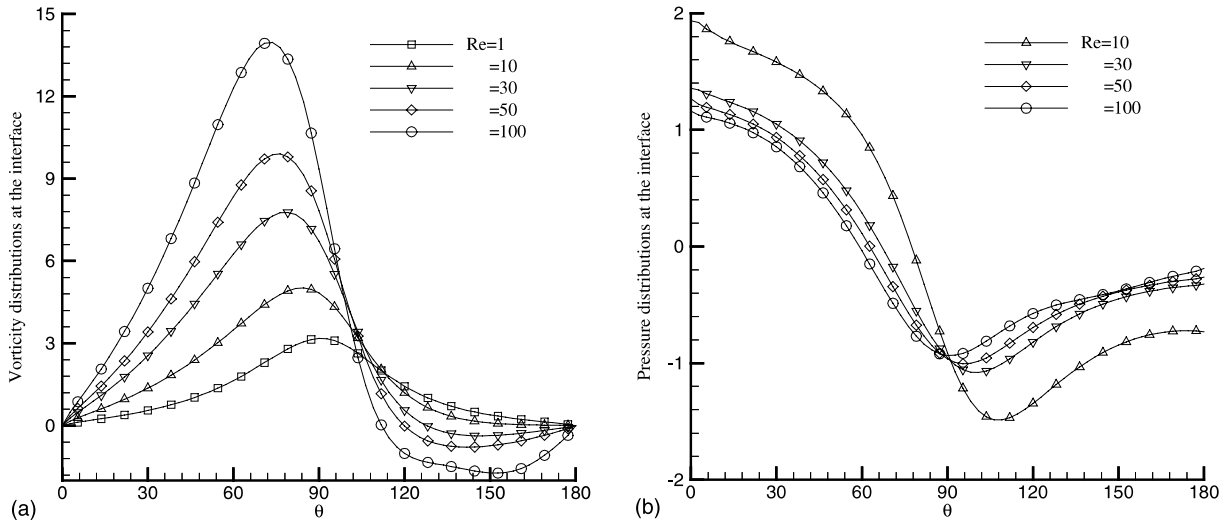

Fig. 15. (a) Surface vorticity distributions for the rigid spheroid at $E = 0.5$. (b) Surface pressure distributions for the rigid spheroid at $E = 0.5$.

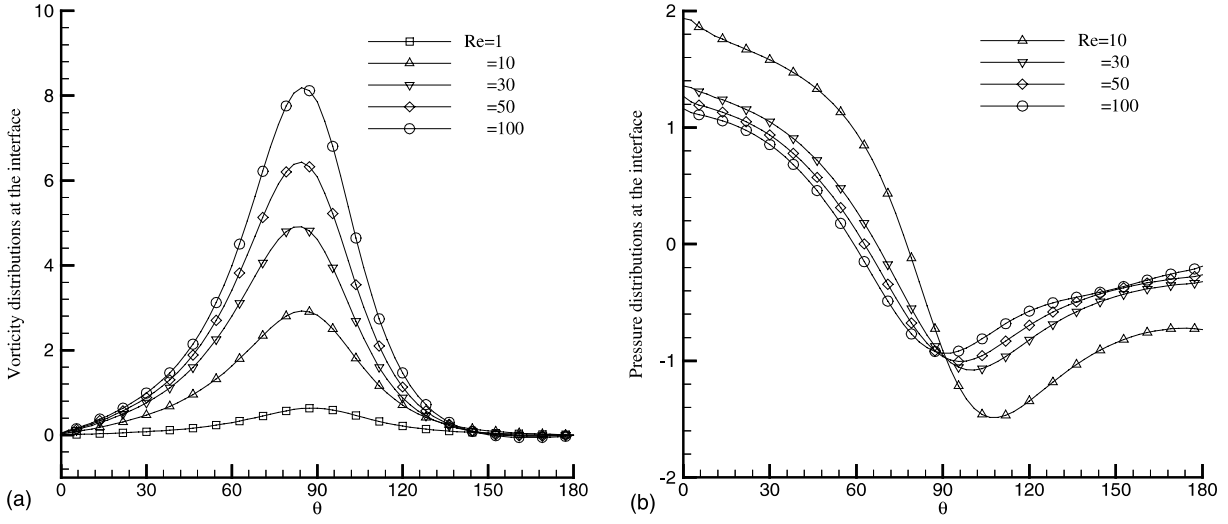

Fig. 16. (a) Surface vorticity distributions for the spheroidal bubble at $E = 0.5$. (b) Surface pressure distributions for the spheroidal bubble at $E = 0.5$.

are identical with the distributions, showing much more symmetry between 60° and 120° for $E = 0.2$, while they are symmetrical between 45° and 135° when $E = 0.5$. However they are increasingly asymmetric for the rigid spheroids. Fig. 17 shows a comparison of the interfacial pressure distributions for inviscid bubbles with different eccentricity at $Re = 100$. The resulting comparison shows a significant effect of bubble geometry on fluid flow at the rear of the bubble. With small eccentricities, such as $E = 0.2$, the profiles of pressure distribution are similar to those

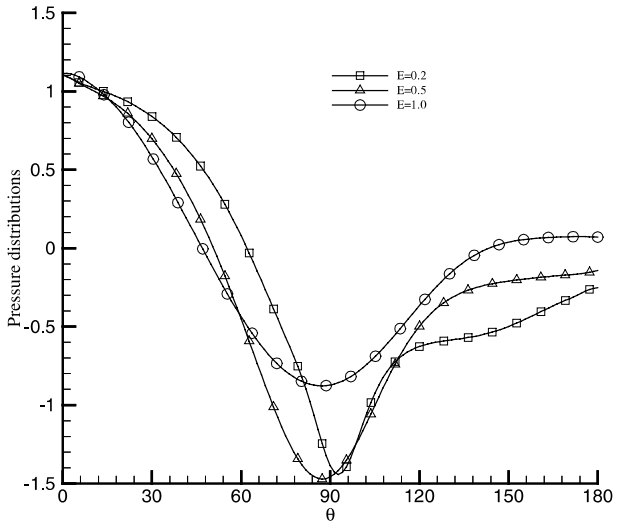

Fig. 17. A comparison of pressure distributions at $Re = 100$.

for rigid spheroids, while when E is greater, e.g. $E = 1.0$, the pressure distribution trends to one of potential flow.

4.3. Drag coefficient and wake length

The drag coefficient for and wake length behind the rigid spheroids and the inviscid spheroidal bubbles are calculated. In this paper, the drag coefficient is defined as $C_D = 2F_x/\rho V^2 \pi B^2$ and calculated by equation

$$C_D = 16 \int_0^1 \left(-p + \frac{2}{Re} \frac{\partial V}{\partial n} \right) r \frac{\partial r}{\partial \xi} \, d\xi; \tag{17}$$

and the wake length is normalised by $2B$. Figs. 18 and 19 show the results and comparisons for rigid spheroids for $E = 0.2$ and 0.5 respectively. It can be seen from Figs. 18a and 19a that the drag coefficients for the bubble are smaller than those for the rigid spheroids. Fig. 18b shows that the wake lengths behind the bubble are bit shorter than those behind the rigid spheroids when E is 0.2. This is because the flow resistance over the bubble is very strong as analysed above. When E is higher, the wake lengths behind the bubble are much shorter than those behind the rigid spheroids as shown in Fig. 19b. In addition to Figs. 18b and 19b present comparisons of wake lengths between our results and Masliyah's results (Masliyah and Epstein, 1970) for rigid spheroids. It can be seen from these figures that they are in very good agreement.

4.4. Local Sherwood or Nusselt number at the surface

Mass and heat transfer characteristics at the bubble interface play an important role in the evolution of a bubble rising in a stagnant liquid, whether hot or cold. The main aim of the present

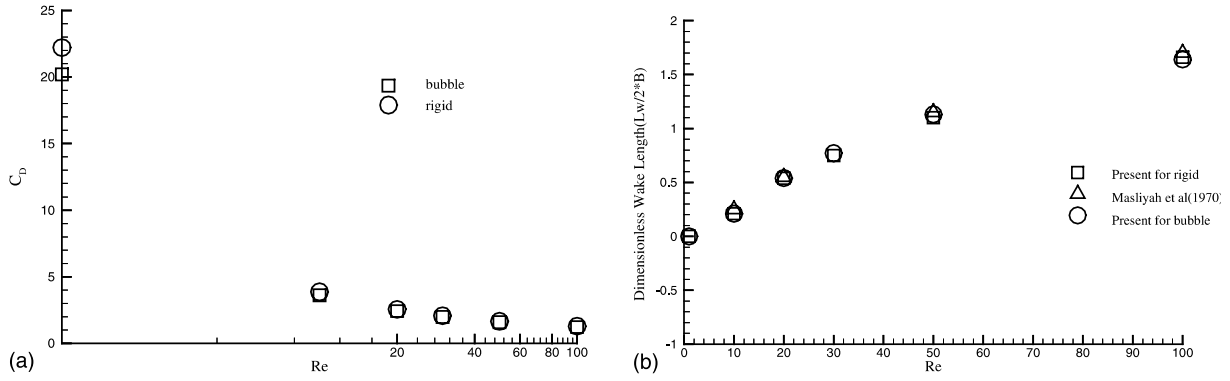

Fig. 18. (a) The drag coefficients for spheroidal particles at $E = 0.2$. (b) The wake length behind spheroidal particles at $E = 0.2$.

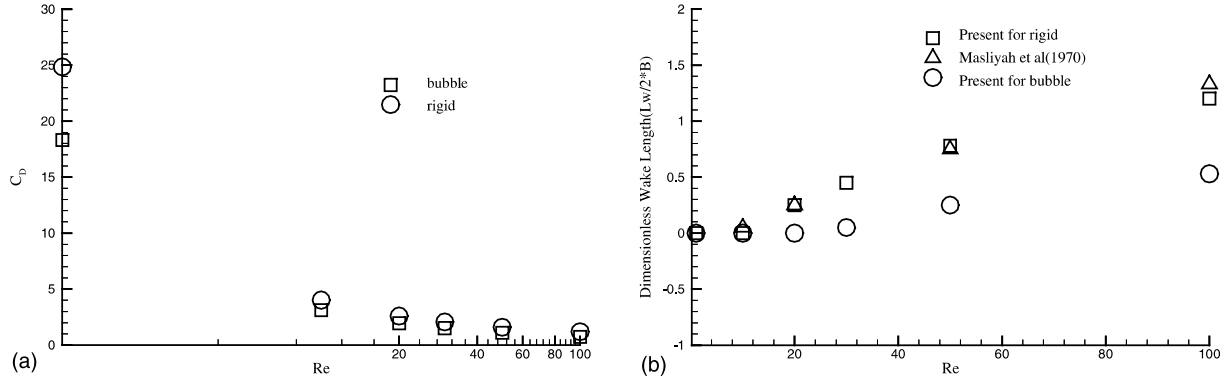

Fig. 19. (a) The drag coefficients for spheroidal particles at $E = 0.5$. (b) The wake length behind spheroidal particles at $E = 0.5$.

study is to establish these characteristics in order to set up a database for further use. The local Sherwood (or Nusselt) numbers at the surface of spheroidal solids and bubbles of $E = 0.2$ and 0.5 are shown in Figs. 20–23 respectively. Where Sherwood number and Nusselt number are defined, respectively, as

$$Sh = \hbar d_e/\aleph, \tag{18}$$

$$Nu = h d_e/\lambda; \tag{19}$$

where $\hbar$, $\aleph$, h and λ stand for mass transfer coefficient, mass diffusivity, heat transfer coefficient and thermal diffusivity respectively. Due to the lack of available experimental data concerning heat and mass transfer, the numerical mass transfer results by Masliyah and Epstein (1972) are employed in the comparison shown in Fig. 5a and b. As stated above, the local Sherwood and Nusselt numbers are equivalent because of the formal analogy between heat and mass transfer

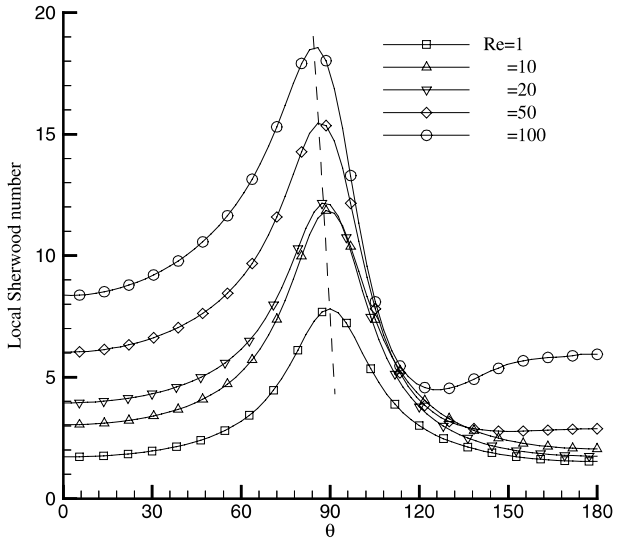

Fig. 20. The local Sherwood number distributions for rigid spheroid at $E = 0.2$.

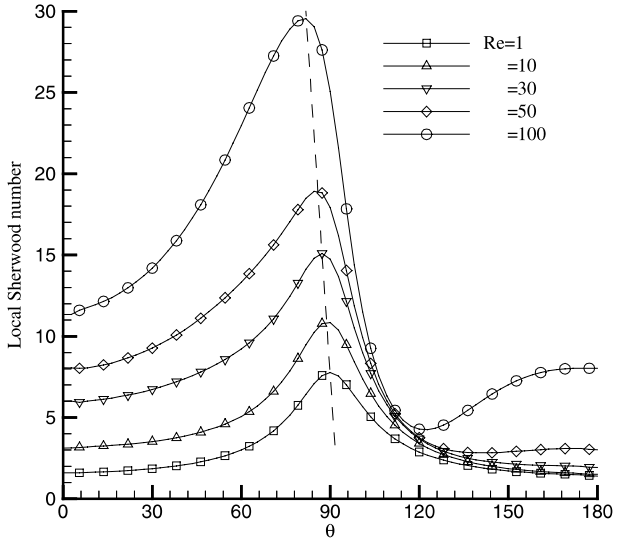

Fig. 21. The local Sherwood number distributions for spheroidal bubble at $E = 0.2$.

under the conditions of the present study. These data can be used to compare with other numerical results on heat transfer. Figs. 20 and 21 show the local Sherwood number distributions for rigid spheroids and spheroidal bubbles. The maximum concentration (or temperature) gradient at the surface is located at angle less than 90° (near the edge of the body). The angle at the maximum gradient decreases with increasing Reynolds number. For spheroidal solids and bubbles, the angle

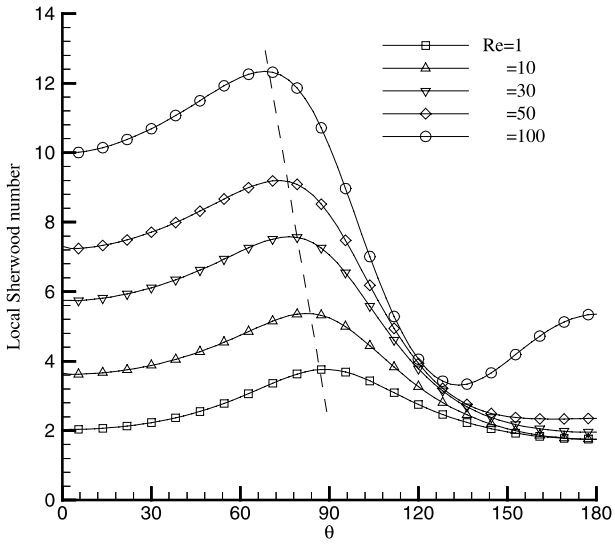

Fig. 22. The local Sherwood number distributions for the rigid spheroid at $E = 0.5$.

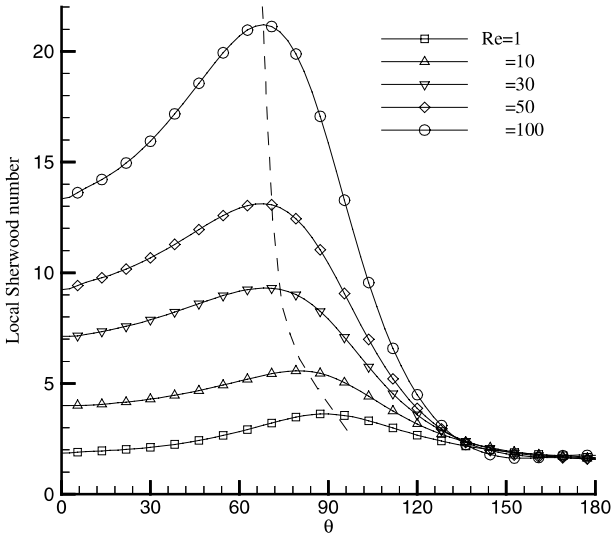

Fig. 23. The local Sherwood number for the spheroidal bubble at $E = 0.5$.

decreases linearly with Reynolds number as the dashed lines shown in Figs. 20 and 21. When *Re* is low, below 100, for both spheroidal solids and inviscid bubbles the Sherwood number increases monontonically with increasing angle around the surface up to a maximum after which it decreases monontonically to a minimum. At high-*Re* ($\sim$100), the change of Sherwood number is different from that when the Reynolds number is low. The Sherwood number reaches a minimum

at a certain angle after which it recovers to a second maximum value. The angle at which the Sherwood number is a minimum changes in a similar way to that of the maximum for both the solid spheroids and for bubbles. The local Sherwood number has two maximum values and a minimum value, and it also has two processes of increase and one decreases at high-*Re*. This is because a separated flow not only occurs at the rear of the rigid sphere, but also develops with an inviscid bubble.

As $E = 0.5$, changes of the local Sherwood number for the rigid spheroid and inviscid spheroidal bubble are basicaly similar to those when $E = 0.2$. The distribution of local Sherwood number is sited between those particles for $E = 0.2$ and 1.0 as shown in Figs. 22 and 23. The difference is that the Sherwood number does not have a larger recovery beyond the angle where it is minimum for inviscid bubble.

In addition, the magnitude of the Sherwood (Nusselt) number for the invisicd bubble is much bigger than that for the rigid spheroid when E is small. This comparison is plotted in Fig. 24. The difference between the Sherwood numbers for the inviscid bubble and for a rigid spheroid is smaller as E increases. The geometry of the bubble clearly has a remarkable effect on the flow and heat or mass transfer characteristics.

The results in Figs. 20–24 highlight the differences between the local Sherwood numbers around an inviscid spheroidal bubble and the rigid spheroid. It should be pointed out that if the bulk liquid is water with a kinematic viscosity of $0.4 \sim 1.0 \times 10^{-6}$ ($m^2\,s^{-1}$) and diffusion coefficient of the solute in the bulk (say oxygen in water) is of $\sim 2.0 \times 10^{-9}$ ($m^2\,s^{-1}$), the *Sc* will evaluate close to 200–500. To simulate the mass transfer to or from an inviscid spheroidal bubble in a liquid at low Reynolds number ($Re = 10$) more realistically, the changes of local *Sh* with *Sc* (which is set at 0.5, 5, 50, 500 and 1000 respectively) and eccentricity parameter E (which is set at 0.2, 0.5 and 1.0 respectively) have been calculated and the results are presented in Figs. 25–27. It can be seen that the distributions of local Sherwood numbers change significantly with Schmidt number and also change with the eccentricity parameter E.

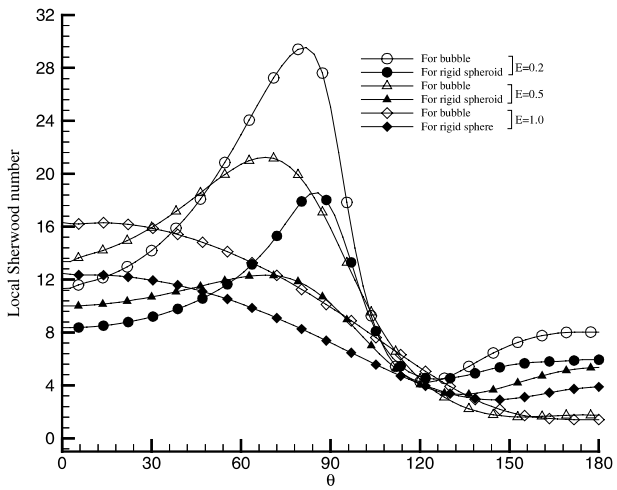

Fig. 24. The comparison of local Sherwood number for particles with different geometry parameter at $Re = 100$.

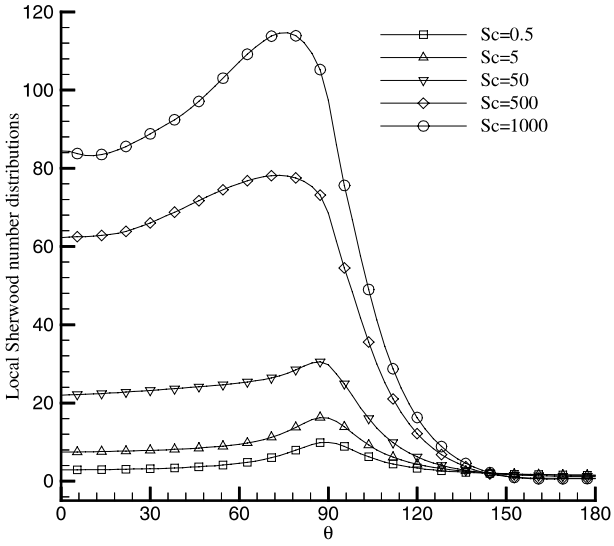

Fig. 25. Local Sherwood number distributions with Schmidt number at $E = 0.2$ and $Re = 10$.

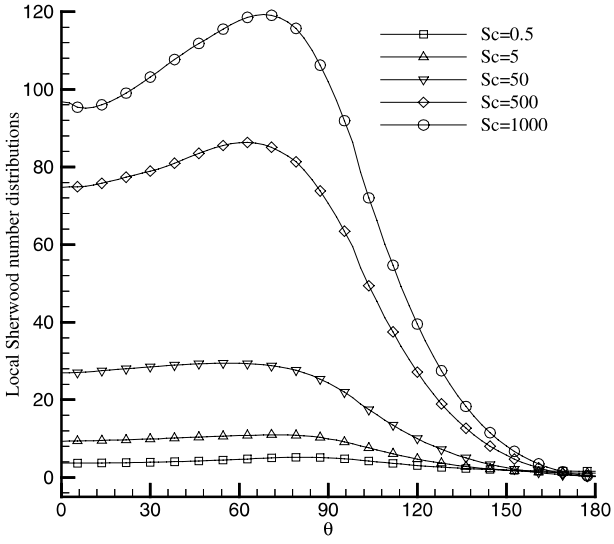

Fig. 26. Local Sherwood number distributions with Schmidt number at $E = 0.5$, $Re = 10$.

4.5. Mean Sherwood number

As a final result for practical application, it is important to get the variation of the mean Sherwood number with the Reynolds and Schmidt numbers and the geometry parameter E. Fig. 28 shows the dependence of the mean Sherwood number upon Reynolds and Schmidt numbers,

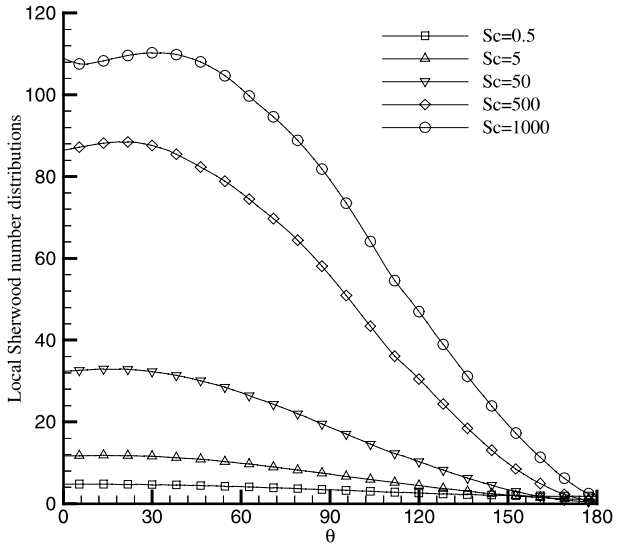

Fig. 27. Local Sherwood number distributions with Schmidt number at $E = 1.0$, $Re = 10$.

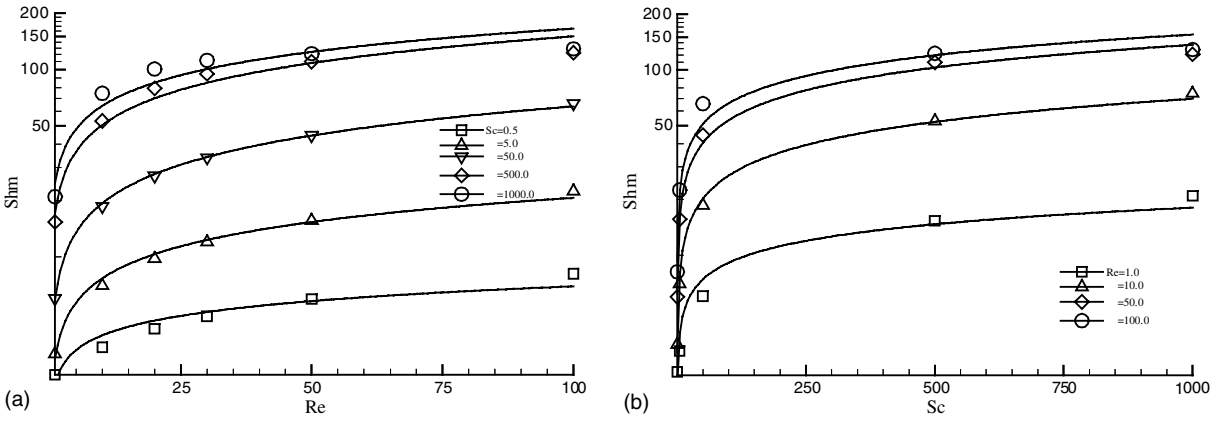

Fig. 28. Mean Sherwood number for $E = 1$.

respectively, for an inviscid spheroidal bubble (at $E = 1.0$). Two types of plots are presented respectively in (a) and (b), one is of *Sh* versus *Re* for different *Sc*, the other is of *Sh* versus *Sc* for different *Re*. Similarly, Figs. 29 and 30 plot final results of mean Sherwood number variation with *Re* and *Sc* for an inviscid spheroidal bubble at $E = 0.5$ and 0.2, respectively. In the above figures, the numerical results are fitted quite well by the continuous curves displayed in the figures; this may be useful for practical prediction. In general, the figures show clearly that the mean Sherwood number increases with the Reynolds and Schmidt numbers; it does not change much with the eccentricity parameter E, even though the local Sherwood number distribution does change with E.

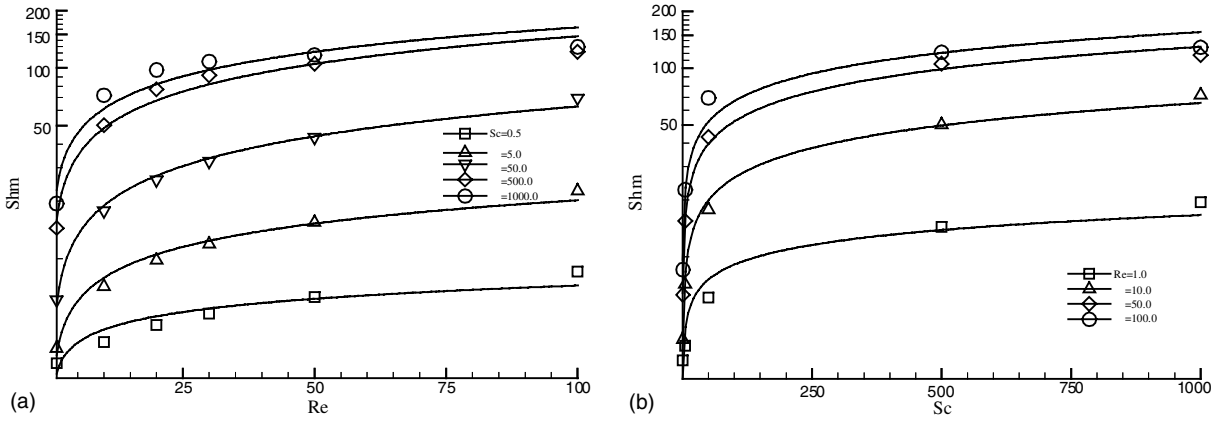

Fig. 29. Mean Sherwood number for $E = 0.5$.

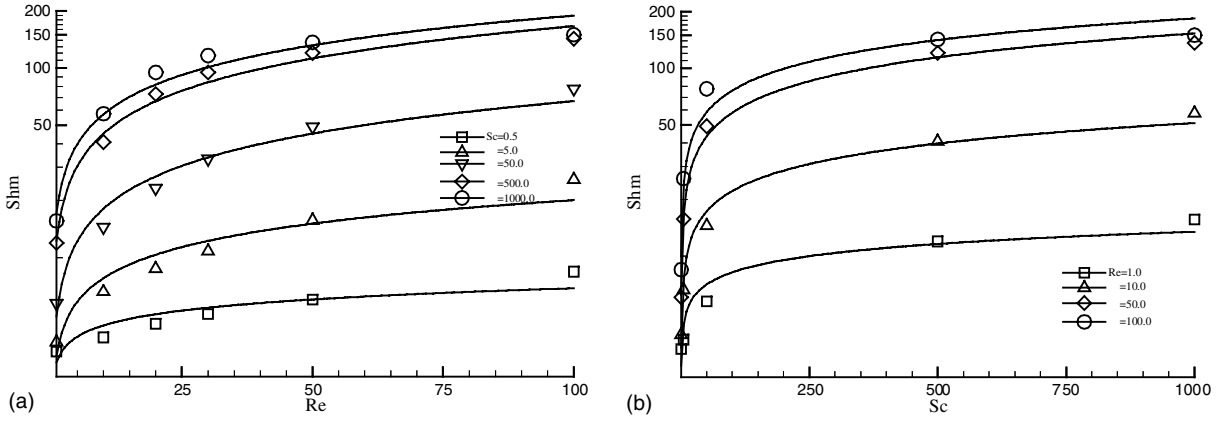

Fig. 30. Mean Sherwood number for $E = 0.2$.

5. Conclusions

In this paper, some results of numerical investigations of steady axisymmetric flow and heat and mass transfer characteristics at the surface of rigid spheroids and inviscid spheroidal bubbles have been presented. The numerical code developed for this study employs a velocity–pressure formulation combined with a finite-volume discretisation of Navier–Stokes, species continuity and energy equations written in non-orthogonal BFCs. Computations have been carried out in the range $10 \leqslant Re \leqslant 300$ for spherical bubbles and rigid spheres in order to cover much of the laminar regime. Due to effect of geometry of spheroidal bubbles and rigid spheroids on flows, Re is only taken up to 100 in order to avoid vortex shedding. In the numerical study, two types of standard flows have been simulated. The numerical results of flows past a rigid sphere and spheroid are in very good agreement with earlier solutions. The numerical results for flow fields

and concentration or temperature fields around rigid spheres and spheroids are also very close to other researchers' results. These comparisons show that the code developed can be used for simulating flows and heat and mass transfer of bubbles. These numerical investigations of the flow and heat mass transfer at rigid spheroids and inviscid spheroidal bubbles with different geometric parameters have several results:

(1) The flows past an inviscid bubble with a small E are asymmetric, becoming increasingly symmetrical for large E. It reveals that the shape of a bubble or rigid body still has a striking effect on the flow.
(2) There is an intrinsic difference between the flow characteristics at the surface of spheroidal particles and bubbles. The wake not only occurs at rear of a rigid particle, but also appears behind an inviscid spheroidal bubble (at $E = 0.2$ for $Re \geqslant 10$ and at $E = 0.5$ for $Re \geqslant 30$). The wake volume at rear of the bubble is smaller than that behind the rigid spheroid at the same Reynolds number. The separation angle for the rigid spheroid is bigger than that for the inviscid spheroidal bubble. In addition, the separation angle for a bubble changes with E at same Reynolds number.
(3) Importantly, the physics involved in the generation of recirculating region is somewhat different for the two types of bodies. For the spheroidal bubble, even though the surface is shear-free, the curvature produces vorticity, whereas on a rigid body surface the vorticity is directly proportional to the local shear. This difference in the way that vorticity is generated at the surface explains why the wake is much longer for a rigid spheroid than for a bubble for given E and Re.
(4) Significant differences in the flow field are reflected in marked differences in the concentration (or temperature) fields for particles with different geometric shapes. The greatest difference is the change in the local Sherwood number profiles between the front stagnation points to the rearmost point of an inviscid bubble. As E is smaller and Re is high, the Sherwood number has two maximum with two increasing and two decreasing regions.
(5) The concentration wake behind a rigid spheroid appears more uniform than that behind an inviscid spheroidal bubble.
(6) To more realistically simulate the motion of an inviscid spheroidal bubble in a real liquid at low Reynolds number ($Re = 10$), the changes of local Sh with Sc (Sc is about 500 if the bulk liquid is water) and eccentricity parameter E have been calculated. The results show that the distributions of local Sherwood numbers change significantly with Schmidt number and also change with eccentricity parameter E.
(7) The numerical results of mean Sherwood number are fitted quite well; the Sherwood number increases with Reynolds number and Schmidt number, but is little influenced by the eccentricity parameter E.

Acknowledgements

The authors wish to acknowledge the support for this work by Nottingham Trent University's Faculty Fund and the UK's Engineering and Physical Sciences Research Council (EPSRC) grant GR/M90207.

References

Cebeci, T., Su, W., 1988. Separation of three-dimensional laminar boundary layers on a prolate spheroid. J. Fluid Mech. 191, 47–77.

Clift, R., Grace, J.R., Weber, M.E., 1978. Bubbles, Drops, and Particles. Academic Press.

Dennis, S.C.R., Walker, J.D.A., 1971. Calculation of the steady flow past a sphere at low and moderate Reynolds numbers. J. Fluid Mech. 48, 771.

Ferziger, J.H., Peric, M., 1999. Computational Methods for Fluid Dynamics. Springer., p. 216.

Fornberg, B., 1988. Steady viscous flow past a sphere at high Reynolds number. J. Fluid Mech. 190, 471–489.

Huang, H., Prosperetti, A., 1994. Effect of orthogonality on the solution accuracy of the two-dimensional convection–diffusion equation. Numer. Heat Transfer, Part B 26, 1–20.

LeClair, B.P., Hamielec, A.E., Pruppacher, H.R., 1970. A numerical study of the drag of a sphere at low and intermediate Reynolds numbers. J. Atmos. Sci. 27, 308–315.

Magnaudet, J., Rivero, M., Fabre, J., 1995. Accelerated flow past a rigid sphere or a spherical bubble, Part 1. Steady straining flow. J. Fluid Mech. 284, 97–135.

Masliyah, J.H., Epstein, N., 1970. Numerical study of steady flow past spheroids. J. Fluid Mech. 44, 493–512.

Masliyah, J.H., Epstein, N., 1972. Prog. Heat Mass Transfer 6, 613–632.

Patankar, S.V., 1980. Numerical Heat Transfer and Fluid Flow. Hemisphere Publishing Corporation.

Patankar, S.V., Spalding, D.B., 1972. A calculation procedure for heat, mass and momentum transfer in three-dimensional parabolic flows. Int. J. Heat Mass Transfer 15, 1787–1806.

Patel, V.C., Baek, J.H., 1985. Boundary layers and separation on a spheroid at incidence. AIAA J. 23, 55–63.

Rimon, Y., Cheng, I., 1969. Numerical solution of a uniform flow over a sphere at intermediate Reynolds number. Phys. Fluids 12, 949–965.

Ryskin, G., Leal, L.G., 1984a. Numerical solution of free-boundary problems in fluid mechanics. Part 1: The finite-difference technique. J. Fluid Mech. 148, 1–17.

Ryskin, G., Leal, L.G., 1984b. Numerical solution of free-boundary problems in fluid mechanics. Part 2: Buoyancy-driven motion of a gas bubble through a quiescent liquid. J. Fluid Mech. 148, 19–35.

Ryskin, G., Leal, L.G., 1984c. Numerical solution of free-boundary problems in fluid mechanics. Part 3: Bubble deformation in an axisymmetric straining flow. J. Fluid Mech. 148, 37–43.

Shyy, W., Udaykumar, H.S., Madhukar, M.R., Richard, W.S., 1996. Computational Fluid Dynamics with Moving Boundaries. Taylor & Francis.

Takagi, S., Matsumoto, Y., 1996. Force acting on a rising bubble in a quiescent liquid. In: ASME Fluids Engineering Division Conference 1. FED-Vol. 236, pp. 575–580.

Takagi, S., Matsumoto, Y., Huang, H., 1997. Numerical analysis of a single rising bubble using boundary-fitted coordinate system. JSME Int. J. B 40, 42–50.

Thomas, P.D., Middelcoff, J.F., 1980. Direct control of the grid point distribution in meshes generated by elliptic equations. AIAA. J. 18, 625–656.

Thompson, J.F., Shanks, S.P., Wu, J.C., 1974. Automatic numerical generation of body-fitted curvilinear coordinate system for fields containing any number of arbitrary two-dimensional bodies. J. Comp. Phys. 15, 299–315.

Tomiyama, A., Sou, A., Zun, I., Sakaguchi, T., 1994. In: Proc. German–Japanese Symp. on Multi-Phase Flow. pp. 847–853.

Wang, Y., Satoru, K., 1999. Comparison of using Cartesian and covariant velocity components on non-orthogonal collocated grids. Int. J. Numer. Meth. Fluids 31, 265–280.

Wang, K.C., Zhou, H.C., Hu, C.H., Harrington, S., 1990. Three-dimensional separated flow structure over prolate spheroids. Proc. R. Soc. Lond. A 421, 73.

Wu, T., Shen, S.F., 1992. Emergence of three-dimensional separation over a suddenly started prolate spheroid at incidence. AIAA J. 30, 2707–2715.

Yan, Y.Y., Li, W.Z., 2002. Numerical investigations of the flow and heat and mass transfer at the interface of a spherical gas bubble. Int. J. Transport Phenom. 4, 209–224.